Available online at www.sciencedirect.com

ScienceDirect

Acta Materialia 90 (2015) 46–58

Acta MATERIALIA

www.elsevier.com/locate/actamat

A synchrotron X-ray diffraction study of in situ biaxial deformation

D.M. Collins,[a,*] M. Mostafavi,[b] R.I. Todd,[a] T. Connolley[c] and A.J. Wilkinson[a]

[a]*Department of Materials, University of Oxford, Parks Road, Oxford OX1 3PH, UK*
[b]*Department of Mechanical Engineering, The University of Sheffield, S1 3JD, UK*
[c]*Diamond Light Source Ltd, Harwell Science & Innovation Campus, Didcot OX11 0DE, UK*

Received 9 December 2014; revised 3 February 2015; accepted 6 February 2015
Available online 6 March 2015

Abstract—The biaxial deformation of a ferritic sheet steel has been examined using high energy in situ X-ray diffraction. A purpose built biaxial loading mechanism was constructed to enable deformation across a wide range of strain ratios. Three nominal deformation conditions were compared: (1) uniaxial loading, $\epsilon_{TD}/\epsilon_{RD} = -\nu$, (2) biaxial deformation where $\epsilon_{TD}/\epsilon_{RD} = 0.4$, and (3) approximately balanced biaxial deformation, with $\epsilon_{TD}/\epsilon_{RD} = 1.5$. This novel setup allowed the full Debye–Scherrer diffraction rings to be acquired during arbitrary selected strain-paths, permitting lattice strains and reflection intensities to be measured across an unrivalled grain orientation range for such deformation conditions. This experiment reveals that the accumulation of lattice strain during deformation, as a function of azimuthal angle, is highly sensitive to strain path. For the $\epsilon_{TD}/\epsilon_{RD} = 1.5$ strain path, whilst lattice strain accumulates most rapidly in the ϵ_{TD} direction during early stages of plastic deformation, the lattice strain is shown to distribute almost perfectly isotropically for the observed orientations when plastic strain is high. This was found to be in contrast to strain paths where $\epsilon_{TD}/\epsilon_{RD} \ll 1.5$, demonstrating that lattice strain magnitudes remain highest in the direction parallel to the tensile axis with the highest applied load. Furthermore, the technique provides the capability to observe the evolution of texture fibres via changes in reflection intensity during different applied strain ratios.

Keywords: Synchrotron radiation; X-ray diffraction (XRD); Biaxial deformation; Texture; Lattice strain

1. Introduction

In a metallic material, deformation cannot be assumed to be accumulated homogeneously at a crystal level. For a single phase metallic material, this inhomogeneity will be influenced by a vast array of factors including crystal structure, grain size, morphology, orientation and distribution, which together influence the yield, plastic flow and failure of the material. The material behaviour is further complicated for a multiphase material where the partitioning and/or localisation of deformation will be influenced by the independent properties of the constituent phases. This inhomogeneous patterning of deformation results in a distribution of stress both at a macroscale (type I) and on a microscale (type II & III) [1]. The mechanical response of a material will be influenced by the superposition of these stress contributions, which if quantified, will help the understanding of deformation phenomena on a crystal scale.

Experimentally, only a limited number of techniques are capable of measuring the deformation at a crystal level. Electron backscatter diffraction (EBSD) [2], X-ray diffraction [3], and neutron diffraction [1] methods can provide suitable measurements of localised deformation. Each method has advantages and drawbacks, and hence a suitable selection will be dependent on the microstructural and/or micromechanical feature of interest, in conjunction with its length scale. EBSD may be used to describe local elastic strains to high sensitivities [4], though these measurements can practically only be made across a limited number of grains. Neutron diffraction has been successfully used to measure the evolution of lattice strains (e.g. [5]) through thick samples. Although in situ measurements are possible, neutron diffraction data collection times are typically too long for dynamic experiments. Testing via high energy synchrotron X-ray diffraction offers rapid data acquisition times with the ability to measure the micromechanical response [6]. However, the sample thickness may be restricted due to energy dependent attenuation.

The micromechanical behaviour of a material when subjected to deformation can be revealed when tested in a uniaxial manner, however, this understanding is unlikely to be satisfactory to explain the response to more complex, multiaxial stresses experienced during fabrication or service. For example, sheet forming operations such as drawing, stamping or stretch forming may subject material to a wide range of biaxial strain paths. Due to the extensive use of such processes for components used in the transport sector, any performance or cost saving benefit from optimisation of sheet forming methods are highly desirable. Improvements may only be exploited when the micromechanical responses are

* Corresponding author.;

http://dx.doi.org/10.1016/j.actamat.2015.02.009
1359-6462/

well understood. Furthermore, understanding residual stresses left after biaxial forming is important due to their potential influence upon component performance in service. By replicating biaxial forming processes experimentally, the knowledge gained can lead to more intelligent component design and manufacture. These measurements may also assist the calibration or validation of models when compared to simulated results [7].

Experimentally, the most obvious way of replicating the biaxial strain paths observed in real components is via the testing of cruciform specimens. However, the number of variables in the geometry is high, making optimisation of the specimen design difficult [8]. In spite of this, examples of successfully testing cruciform specimens do exist (i.e. [9]). Furthermore, experiments that acquire diffraction data from cruciform-type specimens have also been reported. For example, a small biaxial stage designed for thin metallic films of the order of 150 nm thick on polymeric substrates has been installed on the DIFFABS-SOLEIL synchrotron X-ray beamline [10]. Also, a multi-axial test rig has been recently installed onto the neutron time-of-flight diffractometer POLDI allowing deformation of metallic cruciform specimens, as demonstrated with stainless steel [11].

Whilst it is desirable to measure the micromechanical response of biaxial deformation, in practice testing in this manner is far from trivial, as evident from the limited number of biaxial deformation/diffraction experiments reported. Marin et al. [12] used a method of axial loading of a pressurised austenitic steel tube to control the hoop and axial stresses in the material in conjunction with neutron diffraction measurements to obtain lattice strain. An axial strain up to 3–4% was possible. This method has the advantage that the directions of the principal stresses remain constant for different strain ratios, though has a disadvantage that the radial and circumferential stresses vary through the thickness of the tube. A biaxial stress can also be achieved with the application of simultaneous tension and torsion on thin walled tubes in combination with X-ray diffraction (ex situ), [13], though the maximum shear strain was limited to 2% to prevent buckling of the tube. Other examples of X-ray diffraction to measure biaxial deformation include the measurement of an aluminium alloy during deep drawing (reflection diffraction at different orientations) [14], and the use of a Marciniak flat bottom ram [15] to perform balanced biaxial tests [16].

In this study, a purpose built biaxial loading mechanism has been used to enable, for the first time, in situ biaxial deformation measurements from synchrotron X-ray diffraction of metallic sheets. The experiment uniquely enables a rapid rate of data acquisition, recording the full Debye–Scherrer diffraction geometry. This describes the material response across a wide grain orientation range necessary to capture the micromechanical behaviour of a biaxially deforming specimen. This experimental method is shown to be valuable in assessing the deformation response of ferritic sheet steel through a selection of strain paths.

2. Experimental

The deformation of a single phase low carbon ferritic steel, denoted as DX54, has been studied. The nominal composition of this material is given in Table 1. As received, the material had been cold rolled and galvanised with a thickness of approximately 1 mm. Prior to all characterisation in this study, the galvanised zinc coating was removed by abrasive media.

Table 1. Chemical composition of the ferritic steel, DX54 [17].

Element	Fe	C	P	S	Mn
wt.%	Balance	$\leqslant$0.06	$\leqslant$0.025	$\leqslant$0.025	$\leqslant$0.35

The as-received condition of the material was examined using electron backscatter diffraction (EBSD) to characterise the texture, grain size and grain morphology. This was performed using a JEOL-6500F scanning electron microscope, operating at a beam current of 14 nA with an accelerating voltage of 20 keV, and equipped with a TSL/EDAX OIM v6 system. Data were collected with a 1 μm step size over an area of 900 μm × 900 μm and an acquisition time of 0.05 s per pattern. Each diffraction pattern was collected with a 1000 × 1000 pixel camera with 4 × 4 camera binning.

High energy in situ X-ray diffraction experiments were performed on the I12 beamline at the Diamond Light Source. A Shimadzu AGS-X 10 kN load frame was placed on the beamline sample stage orthogonal to the incident X-ray beam. Fitted within this load frame was a bespoke biaxial loading mechanism, based upon a design described by Brieu et al. [18], purpose built for use in this experiment. The rig itself is uniquely capable of deforming a cruciform shaped specimen, simultaneously pulling on all 4 arms to provide a biaxial stress state in the central region of the specimen. To illustrate the movement of the mechanism, computer aided design (CAD) drawings are shown in Fig. 1; in (a) the starting configuration and (b) the final configuration following displacement of the topmost crosshead. In this example, the rig has been configured to provide an equal displacement in the vertical and horizontal directions. However, the diagonal rods, set to 45° in the illustrations shown can be adjusted to change the ratio between the vertical and horizontal displacements, thus changing the strain ratio. A photograph of the biaxial mechanism is shown in Fig. 1(c). During the development of the biaxial loading mechanism, finite element modelling was used, as illustrated in Fig. 2 for example, to assist the mechanism design whilst ensuring the samples were subjected to the desired loading path(s). The design was adapted to ensure that load required to deform the sample would not cause plastic deformation in the rig whilst remaining close the desired strain ratio.

Prior to the experiment, the sample geometry was refined to ensure the sample would deform and fail in the desired region, and that the largest deformation was accommodated in the region where the X-ray beam would pass. The adopted geometry including selected dimensions is shown in Fig. 3(a). The features of the cruciform design can be seen in (a), including broad specimen tabs to fix into grips with pin holes to restrict sample sliding. The combination of waisted specimen arms, a thinned cross-shaped region (on each face of the cruciform) and thinned central disc-shape within the cross permits measurable plastic deformation in the centre of the specimen [19]. In the sections that have been thinned, the corners were chamfered to reduce stress concentrations, mitigating premature failure in these locations. During the design of the specimen, finite element modelling was used to ensure the specimen failure was in the desired location. An example map of Von Mises stress is shown in Fig. 3(b), showing the highest stress will be

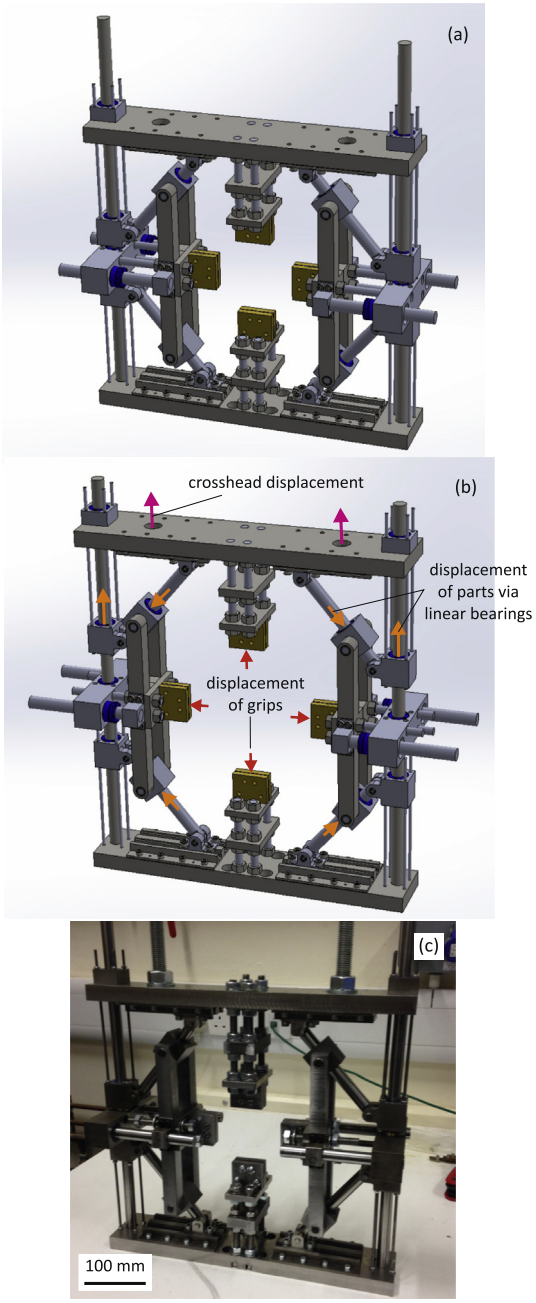

Fig. 1. Biaxial loading mechanism design in SolidWorks in (a) a starting configuration, (b) following displacement of the crosshead, and (c) a photograph of the final rig.

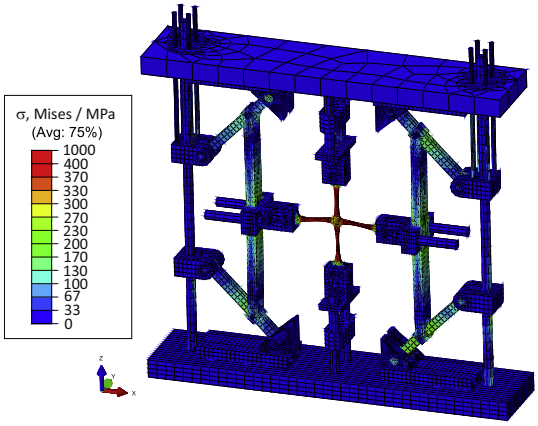

Fig. 2. Biaxial loading mechanism design with Von Mises stress calculation of the rig using finite element modelling.

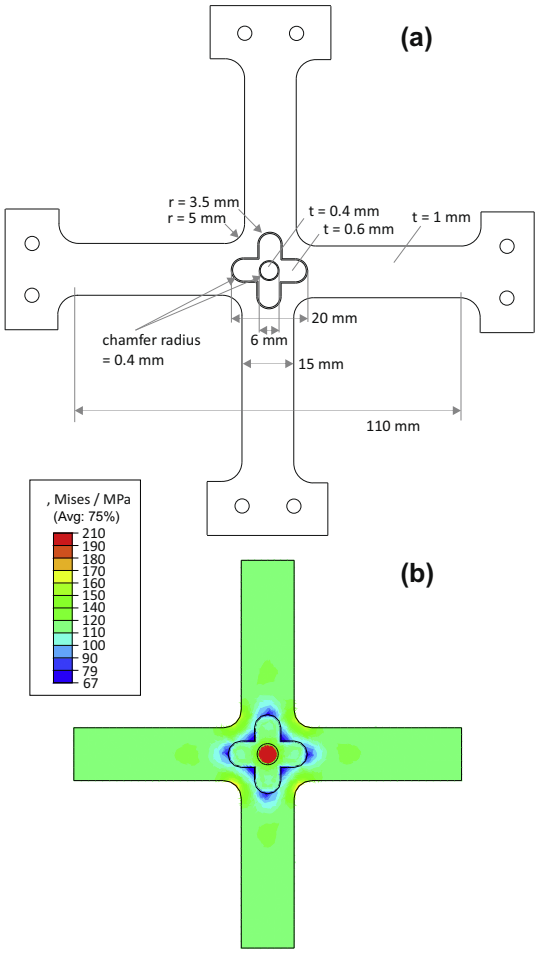

Fig. 3. Cruciform specimen design used throughout the experiment, showing (a) the geometry and important dimensions, noting thickness, t at various locations, and (b) a validation of the stress concentrations using finite element modelling.

experienced in the central thinned region, and that the stress is approximately uniform across this diameter. The material was modelled using mechanical property parameters of yield stress and strain hardening coefficients from independent measurements of DX54 steel [17].

A monochromatic X-ray beam at 90.36 keV ($\lambda = 0.1372$ Å) was used, calibrated with a CeO_2 standard using a method developed by Hart et al. [20]. Diffraction patterns were acquired on a Thales Pixium RF4343 2D area detector with a pixel size of 148 μm and a sample to detector distance of approximately 1125 mm. The data acquisition time per diffraction pattern was fixed at 4 s and the incident beam size was set to 0.5 × 0.5 mm. The spot size was therefore small compared to the central disc of the specimen. An illustration of the experimental setup is shown in Fig. 4.

The acquired diffraction patterns were radially integrated into 36 sectors using the software FIT2D [21]; each

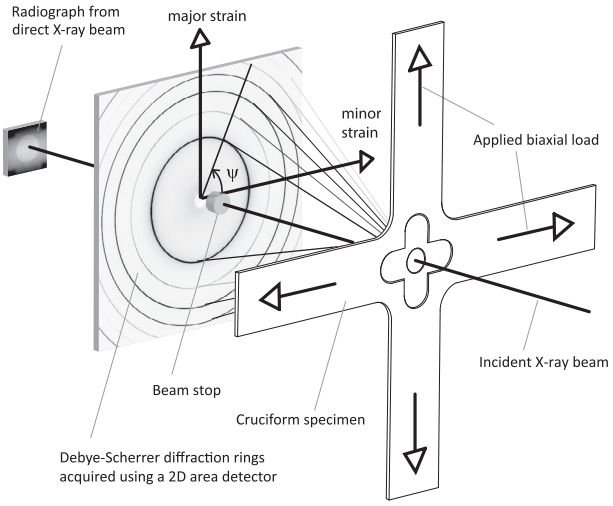

Fig. 4. Experimental setup at the I12 beamline at Diamond, showing the incident X-ray beam striking the cruciform sample which is subjected to biaxial loading. Diffraction data and radiographic images of the gauge volume were acquired with a 2D area detector and imaging detector respectively. For the latter, the beam stop and area detector were temporarily displaced to permit X-ray collection without obstruction.

integrated over a 10° azimuthal rotation. In practice, the sector at an azimuthal angle of ψ, at 0° (integrated between $\psi = -5°$ and $\psi = 5°$), for example, corresponds to the diffracting plane normals within grains that satisfy the Bragg diffraction condition approximately parallel to the minor strain direction ±5° (parallel to the horizontal tensile axis) and the sector at $\psi = 90°$ (integrated between $\psi = 85°$ and $\psi = 95°$) corresponds to diffracting plane normals within grains that are approximately parallel to the major strain direction ±5°. The convention for ψ is also shown in Fig. 4. Single line profile fitting was next performed on selected reflections, namely the {110}, {200}, {211}, {220}, {310} and {222} reflections. This set of reflections were all of the complete diffraction rings acquired during the experiment. These were fitted with a pseudo-Voigt function using algorithms written in the software Matlab. During the fitting of the single diffraction line profiles, a least squares fitting routine was used. The peak position error for each reflection was determined by calculating firstly the Jacobian matrix, and then from this a 95% confidence interval.

During loading of the specimen, as the crosshead of the load rig moves upwards, the central region of interest on the sample also moves upwards. With the beam position remaining fixed, it was necessary to move the sample stage downwards at approximately half the rate of the crosshead, such that the region of interest remained in the beam. As the central thinned region of the cruciform is significantly larger than the beam, the margin of error when doing this (assuming the deformation state within this thinned region does not vary), is quite large. To ensure a sufficient number of grains were sampled when acquiring data during dynamic loading, diffraction patterns were obtained at 4 locations in the thinned region by moving the stage in the plane normal to the incident beam in a square shaped movement through measurements at $y = 0.5$ mm, $x = -0.5$ mm & $x = 0.5$ mm; and at $y = -0.5$ mm, $x = -0.5$ mm & $x = 0.5$ mm. This movement was combined with net downward motion of the sample stage.

In addition to the diffraction detector, an X-ray imaging camera was used, partly as an aid to sample alignment prior to deformation, but also as a tool for observing the deformation of the sample. Loading of the sample was performed in increments, and at each increment radiographs were taken with the X-ray imaging camera, prior to switching back to the diffraction detector. Imaging was performed with a 10 mm × 10 mm incident beam. As the central thinned region of the specimen appears brighter in these images due to greater transmission, measurements of macrostrain could be performed.

The macrostrain of the deformed samples has been measured from radiograph images obtained during interrupted loading intervals. Each radiograph was recorded as 461 × 461 pixels 8 bit images. The macrostrain was calculated using two methods, in each case using a radiograph in the unloaded state as a reference. The methods used were (1) digital image correlation (DIC), and (2) an affine transformation and whole image correlation. Two example radiographs are shown in Fig. 5 in (a) an undeformed state and (b) a deformed state. Here, the higher transmission through the central thinned region can be easily seen, and was the feature used to measure macrostrain.

Digital image correlation analysis was performed using LaVision Strain Master v7.4 [22]. Rigid body corrections were applied to the images before cross-correlation analysis. A preliminary rigid body correction, estimated by visual inspection, was applied to the images; more refined rigid body translations and rotations were eliminated from the displacement fields by an in-house Matlab code (for details of the algorithms used see [23]). Cross-correlation analyses were performed in two stages: in the first stage, 256 × 256 pixel interrogation windows with 75% overlap were used and analysis was carried out in 6 passes; in each pass, the location of the interrogation window was justified based on the displacement field calculated in the previous pass. This was followed, in the second stage, by an analysis with 128 × 128 pixel interrogation windows with 87% overlap and 6 passes. The displacement vectors with correlation coefficient of 0.7 and less were judged to be inaccurate and censored. Lack of contrast features in the empty space surrounding the specimen, resulted in low correlation coefficients (generally lower than 0.3), which was successfully censored using the correlation coefficient criterion. This ensured the strain field was measured in the specimen only. The interrogation windows which satisfied the correlation criterion provided an average strain for this region, noting that there were sufficient features in each window to be tracked. The macromechanical strain in the gauge area

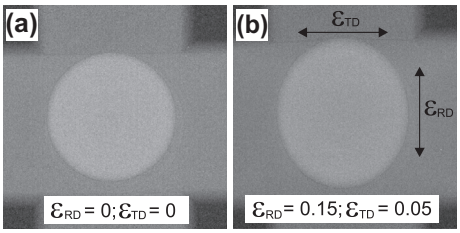

Fig. 5. Example radiographs taken during nominally $\epsilon_{TD}/\epsilon_{RD} = 0.4$ strain ratio testing at (a) prior to deformation and (b) following deformation.

was calculated by averaging the strain field, readily calculated from the full-field displacement, within the bright region evident in radiographs.

For the strains calculated by an affine transformation, a numerical algorithm was used that minimises the difference between the reference image and the radiograph of the deformed specimens after the application of the affine transformation. During each iteration, the deformed specimen radiograph was subjected to a stretch and translation in the vertical and horizontal directions, until a suitable affine transformation was found that has the lowest residual to the reference image. This method assumes a uniform strain across the field so no averaging is needed.

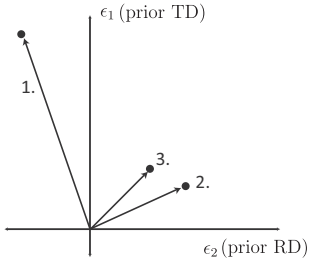

Fig. 7. Strain paths investigated during the experiment following proportional loading of (1) uniaxial, (2) biaxial with $\epsilon_{TD}/\epsilon_{RD} = 0.5$, and (3) balanced biaxial, with $\epsilon_{TD}/\epsilon_{RD} = 1$.

3. Results

The microstructure of the material studied has been characterised using electron backscatter diffraction prior to deformation. An inverse pole figure map of the microstructure is shown in Fig. 6(a) and the corresponding pole figure in Fig. 6(b). The material was found to have a mean grain size of ~20 μm (by area) and a strong texture from previous cold rolling during processing.

During this investigation the deformation behaviour of three distinct strain ratios was investigated. These deformation paths are shown in Fig. 7 where ϵ_{RD} refers to the strain along the original rolling direction of the sheet steel; and ϵ_{TD} refers to the transverse rolling direction. The targeted strain paths were: (1) uniaxial deformation, (2) biaxial deformation biased towards the rolling direction with an approximate strain ratio where $\epsilon_{TD}/\epsilon_{RD} = 0.5$, and (3) balanced biaxial deformation, $\epsilon_{TD}/\epsilon_{RD} = 1$, with strain accumulated equivalently in the rolling and transverse directions.

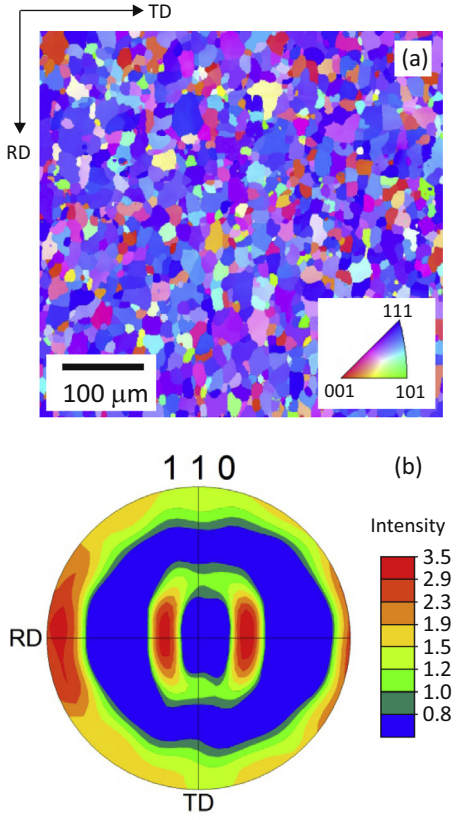

Fig. 6. (a) EBSD inverse pole figure map showing grain structure of DX54 ferritic steel with colours showing crystal directions along the normal direction, ND, and (b) corresponding 1 1 0 pole figure. (For interpretation of the references to colour in this figure legend, the reader is referred to the web version of this article.)

3.1. Macrostrain measurement

The macrostrains for each of the deformed specimens tested are shown in Fig. 8. In general, a reasonable correlation between the two methods of analysing the radiographs is shown, giving suitable confidence of the presented results. The error bars given with the DIC measurements are from root mean square (RMS) values calculated from all interrogation windows that satisfied the correlation criterion. As there was some variation between each of the interrogation windows, the RMS value gives an indication of the strain distribution across each sample and at each stroke displacement increment.

During the deformation, referring to Fig. 8(a), the sample subjected to uniaxial deformation was examined up to a stroke displacement of 25 mm which corresponds to a major strain along the transverse direction of approximately 0.8 and a minor strain along the rollings direction of approximately −0.35, as measured by affine transformation, giving a Poisson's ratio of 0.44, close to the 0.5 value expected for isotropic plastic flow. It is noted that the sample failed in the central disc section between 20 mm and 25 mm of stroke displacement. Reliable DIC measurements were only possible up to 20 mm of stroke displacement, where the tracked features from radiographs from deformations greater than this were too dissimilar from those selected from the reference radiograph. For simplicity, all macrostrain measurements hereon will refer to measurements determined by the affine transformation process.

For the biaxial deformation of samples, the diagonal rods controlling the vertical to horizontal displacement ratio (see Fig. 1) were set to ~27° (i.e $\tan^{-1}(1/2)$) from vertical for a target strain ratio of $\epsilon_{TD}/\epsilon_{RD} = 0.5$, and ~45° for balanced biaxial deformation ($\epsilon_{TD}/\epsilon_{RD} = 1$). The target strain path for the $\epsilon_{TD}/\epsilon_{RD} = 0.5$ strain ratio test were achieved by fixing the specimen with the rolling direction parallel to vertical direction and for balanced biaxial deformation, the transverse direction was parallel to vertical direction.

The measured biaxial macrostrains are shown in Fig. 8(b, c) respectively. These measured strain values indicated that the desired $\epsilon_{TD}/\epsilon_{RD} = 0.5$ strain ratio test was

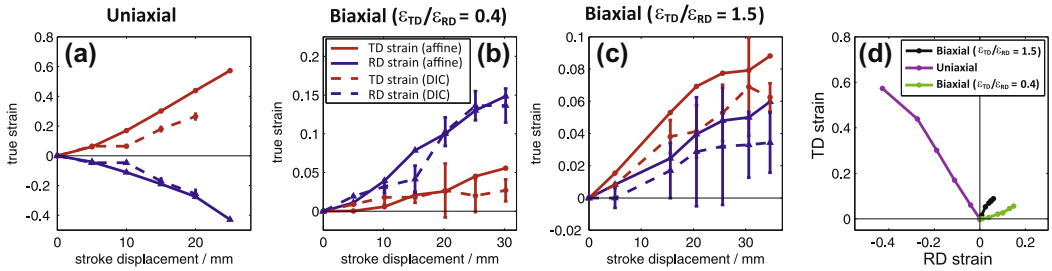

Fig. 8. Macrostrain measurements by DIC and affine transformations for (a) uniaxial loading, (b) $\epsilon_{TD}/\epsilon_{RD} = 0.4$ biaxial, and (c) $\epsilon_{TD}/\epsilon_{RD} = 1.5$ loading.

closer to $\epsilon_{TD}/\epsilon_{RD} = 0.4$ (2 s.f.), and the $\epsilon_{TD}/\epsilon_{RD} = 1$ test had a strain ratio of $\epsilon_{TD}/\epsilon_{RD} = 1.5$ (2 s.f.). From hereon, these measured strain ratios will be used to describe each strain path. For the $\epsilon_{TD}/\epsilon_{RD} = 0.4$ sample, the true strain reached approximately 0.16 along RD before the test was stopped (without failure). However, the true strain achieved for the balanced biaxial test in the TD strain direction was only 0.09 before fracture. The fracture occurred at approximately 30 mm stroke displacement, perpendicular to the major strain direction.

The measured macrostrains with respect to the TD and RD axes for each of the deformation paths are compared in Fig. 8(d). Here, it becomes clear that although the total stroke displacement for each specimen was similar, the plastic strain measured for each strain ratio was significantly different. With no constraint in the minor direction for the uniaxial specimen, a lower force was required to deform the specimens for a given increment in stroke displacement. However, when each of the 4 arms was subjected to simultaneous tension, the design of the specimen dictates a significantly higher force to yield the material. The limited plasticity that is observed by the two biaxial specimens tested arises from the specimen geometry and rig compliance in the horizontal direction, rather than a micromechanical response from the material. This will alter that actual strain ratio and if compliance changes with stroke, this will result in a non-proportional strain path. Specimen geometry is expected to dominate with some strain concentration at the edges of the central thinned region.

3.2. Microstrain measurement

Each sample was subjected to deformation that was controlled by the load frame crosshead displacement, at a constant rate of 0.2 mm min^{-1}. Lattice strains have been calculated using Eq. (1)

$$\epsilon_{hkl} = \frac{d - d_0}{d_0} \tag{1}$$

where ϵ_{hkl} is the lattice strain for the reflection hkl, d_0 is the relaxed reference d-spacing, and d is the measured d-spacing. These lattice strain data are plotted as a function of azimuthal angle (where $\psi = 0°$ is parallel to the minor strain axis, as shown in Fig. 4) and crosshead stroke displacement in Fig. 9. The d_0 values for each of the {110}, {200} and {211} reflections shown were taken from the first diffraction pattern for each specimen prior to loading. Whilst it would be desirable to use an independently

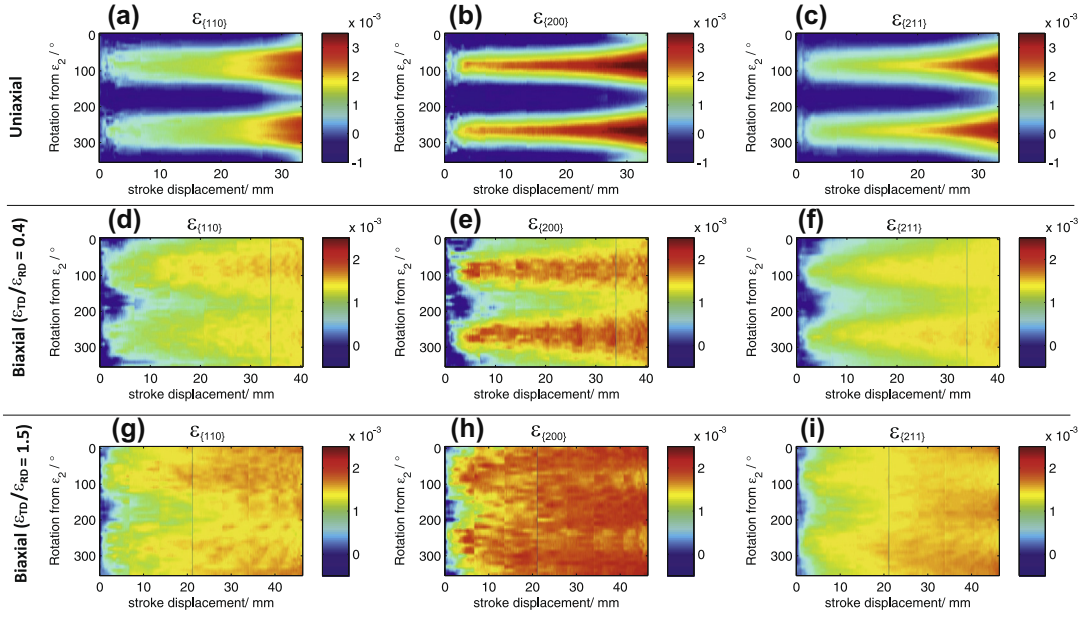

Fig. 9. Microstrain evolution during dynamic loading of samples subjected to proportional deformation, given as a function of azimuthal rotation from the ϵ_{TD} strain direction and stroke displacement. For each sample the lattice strain on the {110}, {200} and {211} planes is shown.

measured d_0 of an annealed reference specimen, the d-spacing error arising from sample misalignment (altering the sample to detector distance) was deemed to be too great to produce reliable absolute measurements of lattice strain. The measurements presented here are lattice strains relative to the initial condition of the specimens.

The lattice strain data are presented in Fig. 9(a–c) for the specimen deformed in a uniaxial manner. The lattice strain for each reflection is shown to increase with stroke displacement for sectors with azimuthal angles close to the vertical major tensile axis along TD. Uniaxial deformation gives a lattice strain reduction in the horizontal minor strain direction. In this example, the tensile axis, described here as ϵ_{TD} is parallel to $\psi = 90°$ and $\psi = 270°$. The minimum lattice strain is shown to be transverse to the tensile axis (ϵ_{RD} direction) at $\psi = 0°, \psi = 180°$ and $\psi = 360°$. Between the presented {110}, {200} and {211} reflections, the two fold symmetry remains present, however, the distribution and magnitude of lattice strain with respect to azimuthal angle is different for each lattice plane.

The lattice strain measurements for the case of biaxial deformation with $\epsilon_{TD}/\epsilon_{RD} = 0.4$ are shown in Fig. 9(d–f). For this sample, TD was aligned along the horizontal axis and so was subjected to the smaller strain. The twofold symmetry displayed by uniaxial deformation remains present, though the distribution and magnitude of lattice strains is now quite different. The lattice strains again accumulate most strongly at azimuthal angles parallel to the largest tensile direction ($\psi = 90°\&270°$) as was the case for the uniaxial test. Notably for each reflection at azimuthal angles close to the ϵ_{TD} direction ($\psi = 0°, 180°\&360°$), the measured lattice strain is now positive whereas for uniaxial deformation, the lattice strain is compressive (this is more obvious in Fig. 11 which is described later). Therefore, for all values of azimuthal angle, the lattice strain increases monotonically as a function of lattice strain. In Fig. 9(e), the magnitude of lattice strain for the {200} lattice plane is shown to be significantly higher than that observed in either the {110} or {211} reflections. This was also the case for the uniaxial test.

Fig. 9(g–i) shows biaxial deformation where $\epsilon_{TD}/\epsilon_{RD} = 1.5$. The magnitude of lattice strain in the azimuthal angles close to each tensile axis (ϵ_{TD}, $\psi = 90°\&270°$ and $\epsilon_{RD}, \psi = 0°$, $180°\&360°$) are almost equivalent, as may be expected when the force exerted in these directions was targeted to be the same. At a stroke displacement of ~25 mm the lattice strain variation with respect to azimuthal angle is negligible, however, this was largely not true for the deformation prior to this. For each of the {110}, {200} and {211} reflections, the lattice strain accumulated more so in the major strain directions ($\psi = 90°$ and $\psi = 270°$). This may be attributed to differing load rig compliances in the two tensile directions. This is quite clear at stroke displacements close to 0 mm where the strain accumulates more rapidly in the vertical loading direction. Whilst the target strain ratio was not achieved, the measured ratio from macrostrain measurement of ~1.5 was sufficiently close for these results to remain highly useful. Beyond ~30 mm stroke displacement, the lattice strain in the horizontal directions ($\psi = 0°, \psi = 180°$ and $\psi = 360°$) becomes greater than that measured in the vertical directions. This is most clearly displayed in Fig. 9(h). This point in the deformation corresponded to necking in the cruciform arms in the major direction, preventing further straining in this direction within the central region of the sample whilst strain continued to increase in the horizontal strain direction. This can be seen in a deviation from the plastic strain path in Fig. 8(c) at higher strains.

Quantitative assessment from the colour plots of the data in Fig. 9 is difficult. For the {110}, {200}, {211} and {310} reflections as a function of azimuthal angle for fixed increments of stroke displacement are given in Fig. 10. Here, stroke displacements at 0, 1, 5 and 25 mm for each of the deformation paths tested are shown. The error bars plotted, associated with peak position uncertainty, are in most cases narrower than the marker

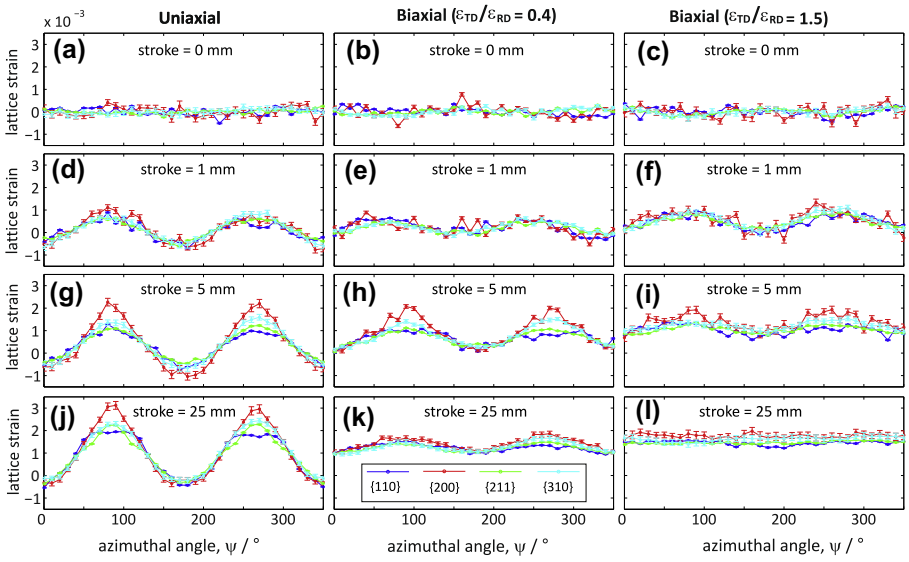

Fig. 10. Microstrain evolution during dynamic loading of samples subjected to proportional deformation, given as a function of azimuthal rotation from the horizontal strain direction and stroke displacement. For each sample the lattice strain on the {110}, {200}, {211} and {310} planes is shown.

points. In general, regardless of the deformation path, when the stroke displacement (and thereby macro strain) is small, i.e. at 1 mm, the measured lattice strain appears approximately the same on each lattice plane. Only when the stroke displacement is higher, does the magnitude of lattice strain vary between the lattice planes. This variation with ψ is most pronounced in uniaxial deformation, and least so for balanced biaxial deformation.

For each deformation path examined at 1 mm stroke displacement, in Fig. 10(d–f), the lattice strain on each plane varies with an approximately sinusoidal function of azimuthal angle. The amplitude of this function appears to be dependent on the applied strain ratio. Deviation from this trend is pronounced at 5 mm stroke displacement and beyond during uniaxial deformation, where sharper minima and maxima appear, firstly in the most compliant {200} lattice plane, then in the {211} lattice plane at greater stroke displacements. The {110} lattice strain, however, appears different. Here, as seen in Fig. 10(f), the lattice strain saturates at $\sim 2.5 \times 10^{-3}$, indicating that all {110} lattice planes from grains with plane normals within a $\sim 60°$ range of the tensile axis have equal lattice strain.

During biaxial deformation, as shown in the second and third columns of plots in Fig. 10, the amplitude of lattice strain variation with azimuthal angle decreases with increasing stroke displacement whilst the mean lattice strain continues to increase. At 25 mm stroke displacement for $\epsilon_{TD}/\epsilon_{RD} = 0.4$ and $\epsilon_{TD}/\epsilon_{RD} = 1.5$ deformation, Fig. 10(k, l) respectively, the maximum deviation of lattice strain from the mean lattice strain is significantly lower than observed for uniaxial deformation. With the $\epsilon_{TD}/\epsilon_{RD} = 0.4$ deformation, the greatest lattice strain remains in a direction parallel to the largest loading axis, as also seen for uniaxial tension, though its magnitude is not markedly greater than for lattice strain at azimuthal angles $0°, 180°$ & $360°$. For balanced biaxial deformation, the lattice strain appears to be homogeneously distributed between grains in all observed orientations. Within experimental scatter, the measured lattice strain for each reflections studied appears to be the same.

The lattice strain information can additionally be observed for azimuthal sectors parallel and perpendicular to the major tensile axis. The source of this diffraction information has been illustrated in Fig. 11(a). These plots are useful as their form is analogous to a macroscopic stress–strain response. In the upper picture, a (2 1 1) lattice plane is shown to be in the Bragg condition with its plane normal, [2 1 1], almost parallel to the vertical tensile axis (TA). Following diffraction from this plane, a diffraction spot will appear at an azimuthal angle of $\psi = 90°$. As the diffraction angle, 2θ is small (i.e. $\sim 6.7°$ for {2 1 1} lattice plane) it is acceptable to assume that the observed lattice strains can be directly compared to macro strain data in the corresponding vertical tensile direction. Likewise, information from lattice planes almost perfectly parallel to the horizontal strain direction, as shown in the bottom illustration of Fig. 11(a), can be extracted. In this case the azimuthal angle, ψ, is $0°$.

Referring to Fig. 11(b–g), the lattice strains are shown as a function of major strain for all reflections examined in this experiment. The coloured bands denote the upper and lower bounds for the measurement uncertainty. Fig. 11(b) shows uniaxial deformation for lattice planes which are perpendicular to the major tensile axis. Each of the shown lattice planes are observed to increase in lattice strain monotonically, though more so for the most compliant {200} lattice plane, as was shown in Fig. 10. In the minor direction, at $\psi = 0$, Fig. 11(e), the Poisson contraction yields a negative lattice strain for all of the studied reflections. Each lattice plane follows a similar trend except the {200} reflection, which is shown to reach -1×10^{-3} before increasing to a lattice strain magnitude similar to the {211} reflection.

For each of the biaxial tests in the vertical tensile direction, $\psi = 90°$, see Fig. 11(c, d), the {200} reflection accommodates the highest lattice strain, as was the case for the uniaxial test. However, this effect becomes less pronounced

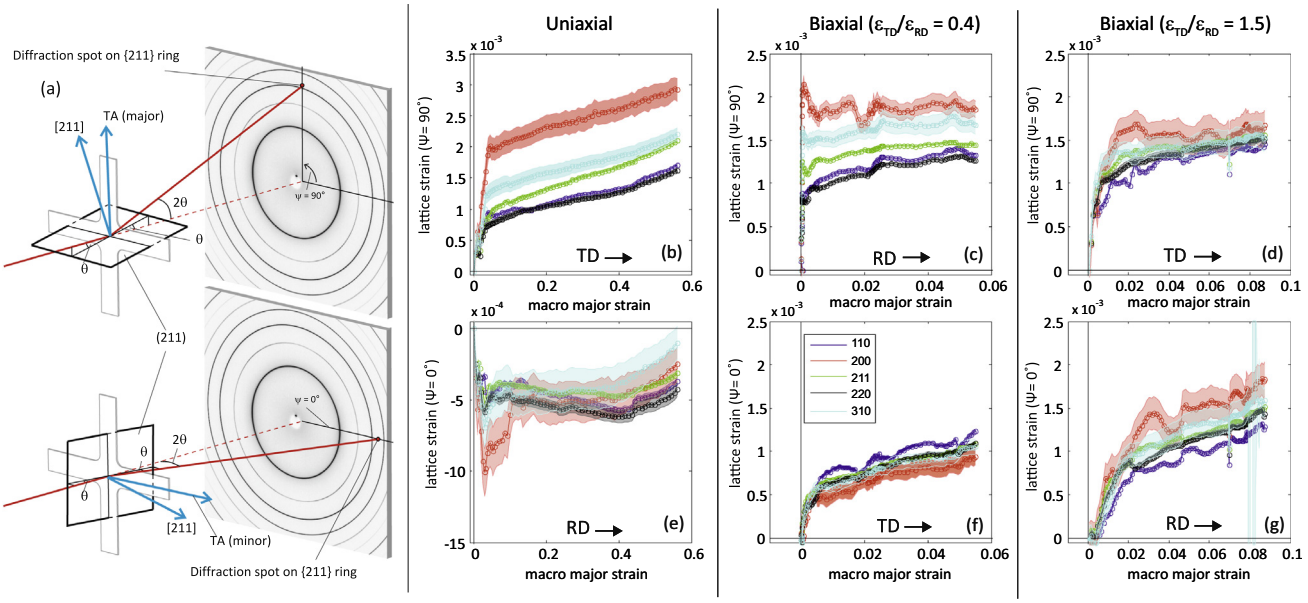

Fig. 11. Microstrain of the {110}, {200}, {211}, {220} and {310} reflections as a function of measured macro strain (obtained from affine transformations). These are shown for the three deformation conditions: Uniaxial Strain, biaxial strain ($\epsilon_{TD}/\epsilon_{RD} = 0.4$) and balanced biaxial strain ($\epsilon_{TD}/\epsilon_{RD} = 1.5$). The rolling and transverse directions, RD and TD, are also labelled.

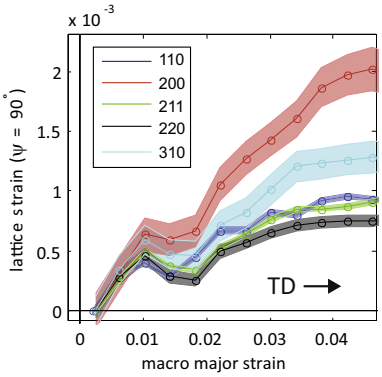

Fig. 12. Lattice strain accumulation at $\psi = 90°$ at low macro strain during uniaxial deformation.

as the strain ratio increases. Evidence of different lattice plane compliances is shown in Fig. 12; taking the example of uniaxial loading at $\psi = 90°$ to demonstrate the different rates of loading prior to yield. In general, the range of lattice strain observed on each of the measured reflections reduces as the strain ratio increases. At $\psi = 0°$ for the $\epsilon_{TD}/\epsilon_{RD} = 0.4$ (Fig. 11(f)) strain path, the compliance ranking of the reflections is approximately reversed from observations at $\psi = 90°$. For the $\epsilon_{TD}/\epsilon_{RD} = 1.5$ sample, Fig. 11(g), the compliance ranking of the reflections is found to be the same in both the $\psi = 0°$ and $\psi = 90°$ azimuthal orientations.

3.2.1. Intensity and texture change

The intensity of the measured reflections has been examined as a function of the stroke displacement, as shown for selected peaks in Fig. 13. From the identified reflections, the plotted values display the numerically integrated intensity across the line profile with the background intensity subtracted. The reflection intensities at zero stroke displacement represent the initial texture of the material. A twofold symmetry is visible in the {1 1 0} with the highest intensity at the 0°, 180° and 360° azimuthal angles from ϵ_{RD} in $\epsilon_{TD}/\epsilon_{RD} = 1.5$ and uniaxial samples. The vertical major tensile axis was parallel to the transverse direction. The $\epsilon_{TD}/\epsilon_{RD} = 0.4$ test has its highest intensity at 90° and 270°, i.e. with the major strain parallel to the rolling direction. As stated previously, this was due to the sample being loaded at 90° to the other 2 samples.

Considering firstly uniaxial deformation, Fig. 13(a), the initial twofold symmetry from the {1 1 0} reflection is present until approximately 3 mm stroke displacement, corresponding to ~0.05 macro strain (major). Beyond this, grain reorientation changes the material texture significantly to yield a 6-fold symmetry which is clearly present by ~10 mm stroke displacement (0.17 major strain). For the same reflection, but in the case of both the $\epsilon_{TD}/\epsilon_{RD} = 0.4$ and $\epsilon_{TD}/\epsilon_{RD} = 1.5$ tests, in Fig. 13(e, i), the intensity of the {1 1 0} reflection with respect to azimuthal angle remains largely unchanged.

When considering the reflections with a higher index, the intensities were significantly lower than that measured for the {1 1 0} reflection (by ~2 orders of magnitude). In the $\epsilon_{TD}/\epsilon_{RD} = 1.5$ and $\epsilon_{TD}/\epsilon_{RD} = 0.4$ tests, the measured intensity changes were small. The {2 0 0} reflection displayed no strong intensity for a given azimuth prior to deformation, though for uniaxial deformation the significant grain reorientation resulted in higher intensity at 60°, 120°, 240° & 300° azimuthal angles, as shown in Fig. 13(b). The 6-fold symmetry observed when the stroke displacement reached ~22 mm corresponds to the fracture strain of ~0.5. As the fracture appeared perpendicular to the tensile axis, though only propagated through the central thinned region of the specimen, deformation was still accumulated in the sample. With the presence of the crack, the loading condition must have been different in the region of interest. Without the ability to specify the precise location of the incident X-ray beam with respect to the crack, no reliable

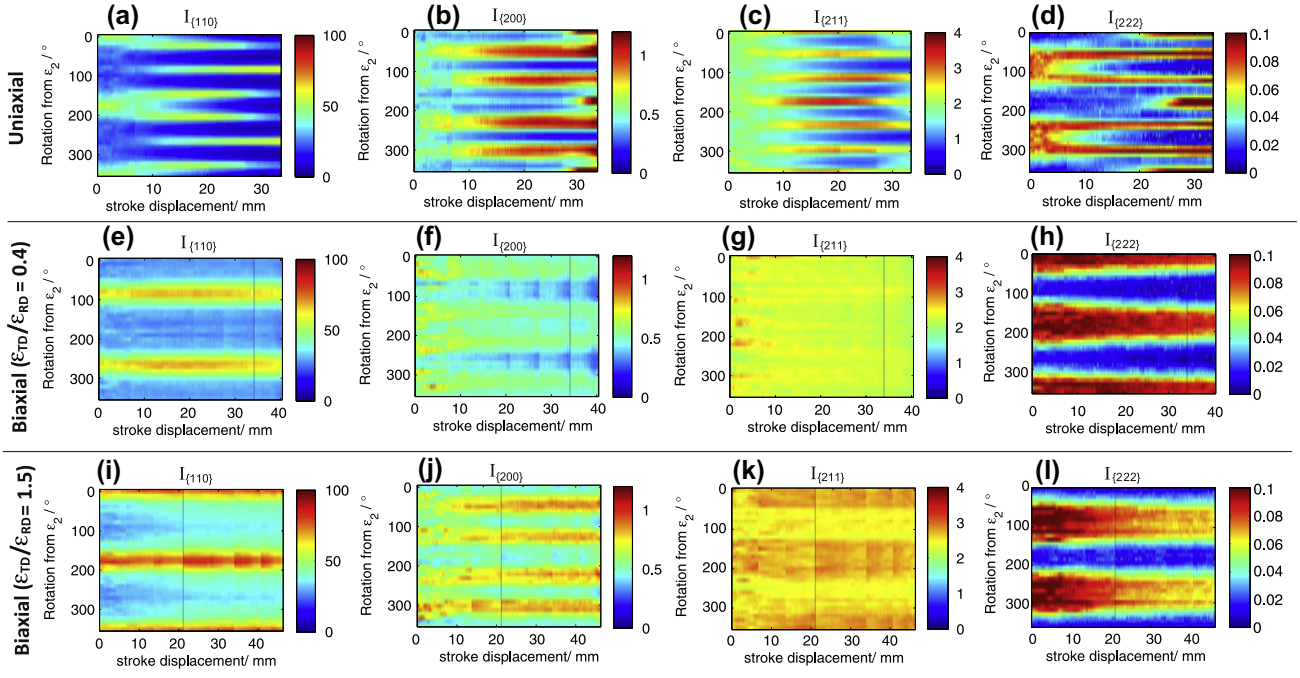

Fig. 13. Intensity change during proportional deformation as a function of azimuthal rotation from the ϵ_{TD} strain direction and stroke displacement for the {1 1 0}, {2 0 0} and {2 1 1} lattice planes.

conclusions can be drawn from the observed intensity change beyond a stroke displacement of 22 mm. Notably however, the change in texture observed here is not accompanied by any abrupt change in lattice strain (i.e. in Fig. 9(a–c). Likewise, the intensity of the {1 1 0} and {2 1 1} reflections do not change dramatically in this period.

The intensity periodicity observed of the {2 0 0} reflection for the $\epsilon_{TD}/\epsilon_{RD} = 1.5$ example in Fig. 13(j) displays little difference to the uniaxial deformation example. It is noted that at ~35 mm stroke displacement the true plastic major strain is ~0.09, with the equivalent plastic strain in the major direction for the uniaxial test is reached at 6 mm stroke displacement. The $\epsilon_{TD}/\epsilon_{RD} = 1.5$ sample had some plasticity occurring in the arms of the cruciform throughout the deformation which did not occur in the uniaxial test, so that a plastic strain comparable to the uniaxial test requires a much greater stroke displacement in the biaxial test. Up to this macrostrain, the {2 0 0} intensity variation does depend on the applied strain ratio. However, for the $\epsilon_{TD}/\epsilon_{RD} = 0.4$ strain ratio, in Fig. 13(f), almost no variation with azimuthal angle is observed. The intensity variation for this reflection therefore must be somewhat dependent on the applied strain ratio, however, the starting texture was different for this case, as the sample was rotated by 90°.

The {2 1 1} reflections in Fig. 13(c, g, k) did not initially display any marked preferential intensity with respect to azimuthal angle. The intensity symmetry developed during uniaxial deformation appeared to be similar to the {1 1 0} reflection though was shifted by $\psi = 30°$, which is also equal to the angle between the two plane normals. A two fold symmetry developed in the $\epsilon_{TD}/\epsilon_{RD} = 1.5$ {2 1 1} reflection, though the amplitude of this variation was significantly less than for the uniaxial case. The symmetry here is the same as the {1 1 0} reflection, though rotated by $\psi = 30°$. Finally, for $\epsilon_{TD}/\epsilon_{RD} = 0.4$ deformation, no notable change in {2 1 1} intensity was observed.

For specimens deformed in a biaxial manner, evidence of texture change can found from an assessment of the {2 2 2} reflection intensity, as shown in Fig. 13(h, l). The initial intensity variation with azimuthal angle shows a 2-fold symmetry, similar to the {1 1 0} reflections, though rotated by 90°. This peak intensity is shown to reduce throughout the deformation, and more so in the $\epsilon_{TD}/\epsilon_{RD} = 1.5$ example. The strong intensity change of this reflection compared to others indicates that this effect is due to texture, rather than an artefact of sample thinning.

4. Discussion

4.1. Sources of error

Variation in the sample to detector distance is perhaps the largest source of error between samples. This will result in a reflection shift, changing value of 2θ to $2\theta'$ through the following expression

$$2\theta' = \tan^{-1}\left(\frac{D+\delta D}{D}\tan(2\theta)\right) \quad (2)$$

where D is the sample to detector distance and δD is its error. An independent X-ray diffraction measurement of a stress-free annealed DX54 specimen reference gives the correct lattice parameter to be 2.8684 Å. An estimate of the displacement error for each specimen can be calculated by rearranging Eq. (2) and using the d-spacing values used in this study. The displacement errors are found to be −0.79 mm, −0.24 mm and +0.03 mm for the uniaxial, biaxial $\epsilon_{TD}/\epsilon_{RD} = 0.4$ and biaxial $\epsilon_{TD}/\epsilon_{RD} = 1.5$ specimens respectively.

To illustrate the validity of using a reference from each specimen, a strain measurement can be recalculated from the corrected sample to detector distance and using the absolute a_0 of 2.8684 Å. As an example, the greatest measured lattice strain from the uniaxial specimen, $\sim 3 \times 10^{-3}$ from the {2 0 0} lattice plane, is recalculated to instead give 3.006×10^{-3}. The difference is deemed to be sufficiently small, and notably within the error associate with peak position fitting (see Fig. 11).

Sample to sample thickness variations will result in different peak intensities at zero stroke displacement for each sample. This is evident in the $\epsilon_{TD}/\epsilon_{RD} = 0.4$ compared to Fig. 13(e–h) and $\epsilon_{TD}/\epsilon_{RD} = 1.5$, Fig. 13(i–l), showing lower respective peak intensities due to a thinner cross section. Additionally, the absolute thickness of the sample will limit the number of diffracting grains. It is noted that of the illuminated volume, only a small fraction of grains will lie within the narrower orientation range that satisfies Bragg's law, thereby drastically reducing the number of grains from which measurements are obtained. Though none of the diffraction patterns appeared spotty, an indication that too few grains are diffracting, the serrations observed in lattice strain measurements, shown in Fig. 11 are likely to be due to limited number of grains studied. As the location of the X-ray beam within the central thinned region of the sample was not fixed throughout the deformation (due to sample movement), grains with differing lattice strains would be entering and exiting the illuminated volume throughout each test. As the grain subset changes, variations in lattice strain may be expected, though are present due to specimen geometry constraints rather than a bulk micromechanical response.

4.2. Lattice strain and intensity trends

The distinctive lattice strain behaviour captured in this experiment for different loading paths reveals that for a given lattice plane, its lattice strain is critically dependent on (1) the orientation of the grain, and (2) the applied strain ratio. These differences have been illustrated in Figs. 9 and 10 for the lattice evolution of the {1 1 0}, {2 0 0} and {2 1 1} lattice planes during loading. The application of a plastic strain which does not have a strain ratio close to that of balanced biaxial deformation will give rise to the transformation of initially circular to a characteristic elliptical diffraction ring shape. Evidence of this can be seen in Fig. 10; from initially no lattice strain variation with azimuthal angle at stroke displacement = 0, when the specimens are deformed an approximately sinusoidal distribution of lattice strain as a function of azimuthal angle is shown. Deviations from this behaviour have been observed at high plastic deformations in the case of the {2 0 0} reflection, where the lattice strain accumulates more so in the direction of the major tensile axis compared to other lattice planes. The differing behaviour was observed in the {1 1 0} lattice plane, where a similar magnitude of lattice strain is distributed across a broad range of azimuthal angles close to the tensile direction. The amplitude of the

observed sinusoidal lattice strain behaviour and the differences between the lattice strain on each lattice reduce significantly with the application of two applied strain directions (for the $\epsilon_{TD}/\epsilon_{RD} = 0.4$ case), and is least prevalent when the biaxial ratio is approximately balanced. This was most evident in Fig. 10(i) where there is no discernible difference between (1) the magnitude of lattice strain on each plane and (2) the variation in lattice strain with respect to plane (and thereby grain) orientation.

Similar in-plane stiffness trends have been observed by Dutta et al. [24] on ferritic steel, noting the {200} lattice plane was significantly more compliant than the {110} and {211} lattice planes. The single crystal plane specific stiffness, E_{hkl} may be described using [25]

$$\frac{1}{E_{hkl}} = S_{11} - 2\left(S_{11} - S_{12} - \frac{1}{2}S_{44}\right)A_{hkl} \tag{3}$$

where S_{ij} is the reduced notation for the single crystal compliance tensor, and A_{hkl} is a plane specific anisotropy factor for a cubic crystal system, given by

$$A_{hkl} = \frac{h^2k^2 + k^2l^2 + l^2h^2}{\left(h^2 + k^2 + l^2\right)^2} \tag{4}$$

where h, k and l are the lattice plane Miller indices. In the tensile direction during uniaxial deformation, the relationship given in Eq. (3) has been widely reported to be true in similar low carbon steels, i.e. [26,27]. As biaxiality is introduced and is increased (as $\epsilon_{TD}/\epsilon_{RD} \rightarrow 1$) the lattice strain difference decrease, replicating the result observed by Marin et al. [12] in stainless steel. The results from this investigation demonstrate this trend is true for a wide range of grain orientations. Using the equations above for known compliance constants in iron [28], the single crystal plane specific stiffness yields 223, 134, 223, 156 GPa for the {110}, {200}, {211}, & {310} lattice planes respectively. The ranking of these stiffnesses can be compared to the ranking of lattice strain magnitudes observed in this study. For this reason, the most compliant {200} lattice plane consistently has the highest strain magnitude and the converse is true for the least compliant {110}, {211} and {220} lattice planes studied. Caution must be taken when using such stiffness values in comparison to a polycrystalline response as the combination of a grain in an elastically soft orientation would be constrained by an adjacent grain if it lies in a hard orientation. Thus, significantly reducing the measured difference between stiffnesses on each lattice plane, as experimentally determined by diffraction elastic constants. In a similar ferritic steel, at room temperature, these are reported as 213, 169 and 222 GPa for the {110}, {200} and {211} lattice planes [24]. These measurements are in agreement to the lattice plane compliances observed during initial elastic deformation, as shown for uniaxial deformation in Fig. 12.

The varying lattice strain with respect to azimuthal orientation, i.e. Fig. 10, and the magnitude of deviation (from the different strain ratios tested) can be explained by resolving a global stress state onto lattice planes in the crystal frame for which the diffraction measurements are made. The global stress, $\underline{\underline{\sigma_s}}$, in the sample frame is given by

$$\underline{\underline{\sigma_s}} = \begin{pmatrix} \sigma_H & 0 & 0 \\ 0 & \sigma_V & 0 \\ 0 & 0 & 0 \end{pmatrix} \tag{5}$$

where σ_V and σ_H are the applied vertical and horizontal stresses respectively. The stress in the crystal frame, $\underline{\underline{\sigma_c}}$, is given by the following rotation

$$\underline{\underline{\sigma_c}} = \underline{\underline{R}}\,\underline{\underline{\sigma_s}}\,\underline{\underline{R}}^T \tag{6}$$

where $\underline{\underline{R}}$ describes the crystal orientation. This matrix of diffracting crystal can be constructed from a 2θ rotation from the diffracting plane Bragg angle, an azimuthal rotation ψ around the Debye–Scherrer ring, and γ, a rotation about the diffraction plane normal ($0° \leqslant \gamma < 360°$). Lattice strains can calculated from the stress vector ($\underline{\underline{\sigma_c}} \rightarrow \underline{\underline{\sigma_c}}$), through

$$\underline{\epsilon_c} = \underline{\underline{S_c}}\,\underline{\underline{\sigma_c}} \tag{7}$$

where $\underline{\underline{S_c}}$ is the reduced compliance tensor for iron. The resulting lattice strains for the {110}, {200}, {211} and {310} lattice planes are shown for uniaxial, $\epsilon_{TD}/\epsilon_{RD} = 0.5$ and $\epsilon_{TD}/\epsilon_{RD} = 1$ strain states in Fig. 14. The stress level used were $\sigma_V = 210$ MPa & $\sigma_H = 0$ MPa for uniaxial, $\sigma_V = 210$ MPa & $\sigma_H = \sigma_V(2+\nu)/(1+2\nu)$, giving $\epsilon_1/\epsilon_2 = 2$, equivalent to the $\epsilon_{TD}/\epsilon_{RD} = 0.5$ strain path from this experiment. Finally, $\sigma_V = 210$ MPa & $\sigma_H = 210$ MPa, giving the $\epsilon_1/\epsilon_2 = 1$ (equivalent to $\epsilon_{TD}/\epsilon_{RD} = 1$) strain path. These stresses provided a maximum bulk strain of 1×10^{-3}. The colour maps show the

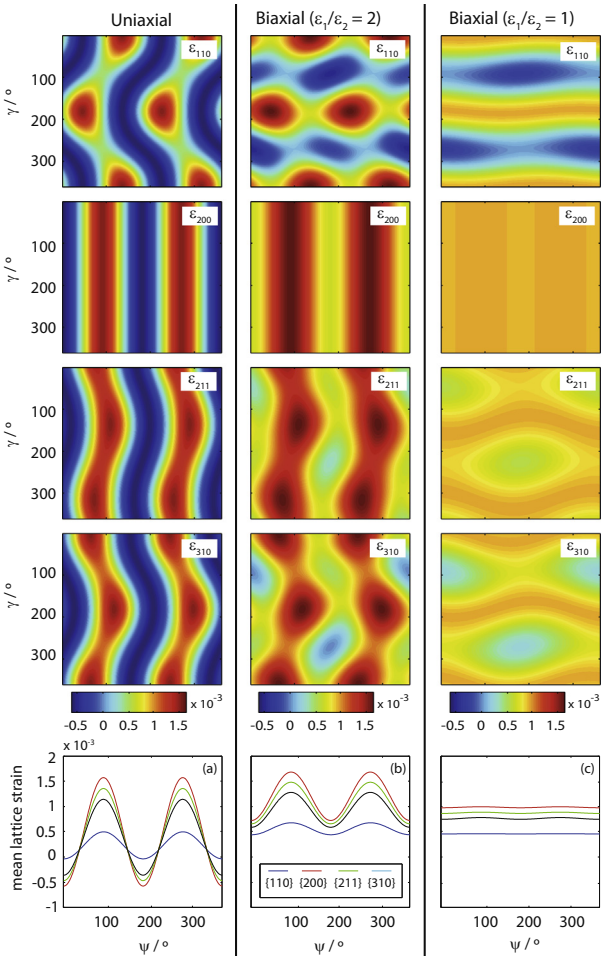

Fig. 14. Calculated lattice strains at a fixed stress for different strain ratios.

variation in lattice strain for each lattice plane with respect to the angles ψ and γ. In practice, the experimentally determined lattice strain will combine measurements from crystal orientations with differing values of γ, but cannot distinguish between them. The measured lattice strain for each value of ψ is therefore an average about γ. The calculated mean lattice strain for the differing strain paths is shown in Fig. 14(a–c), taking the strain tensor component in the direction parallel to the diffracting plane normal from $\underline{\epsilon_c}$.

Though such calculations predict the elastic response prior to yield only, some features of the calculated variation in lattice strain with azimuthal angle are shown to corroborate well with the microstrains shown in Figs. 10 and 11. Notably, the {200} reflection is shown to be the most compliant lattice plane shown, exhibiting the largest lattice strain, and others with a lower compliance are ranked in similar order experimentally. At $\psi = 0, 180$ & 360° for the $\epsilon_{TD}/\epsilon_{RD} = 0.4$ specimen, the lattice strain is predicted to be almost equivalent for each lattice plane, as shown throughout the plastic deformation, Fig. 11(f). For the $\epsilon_{TD}/\epsilon_{RD} = 1.5$ specimen, the actual strain ratio predicts observable variation with azimuthal angle (Fig. 14(c), which is shown experimentally during the early stages of deformation (i.e. Fig. 10(c)), though the trend does not hold during higher levels of plasticity. The predicted elastic response therefore provides a good indicator of the accumulation of lattice strain at low levels of plasticity, though deviates beyond this at greater plastic strains.

The magnitude of elastic strain measured is a function of the plane specific stiffness, and beyond yield, is function of the initial critical resolved shear stress and Schmid factor for the deforming grains in the Bragg condition in conjunction with the hardening as the dislocation density increases. The change in strain distribution as a function of azimuthal orientation throughout the deformation, for each strain path, must vary with the evolution of texture with grain orientation, as the stress state on each grain changes as a function of macrostrain. With this complexity, simple calculations alone are unlikely to explain the observed response at high plastic strains, thus necessitating detailed modelling activities as future work.

The reflection intensities described in Fig. 13 reported clear symmetry changes throughout the deformation paths, indicative of texture change. If one considers the expected texture change in a BCC material, during uniaxial tension a ⟨110⟩ fibre develops, and for uniaxial compression, mixed ⟨100⟩ and ⟨111⟩ fibres form [29]. During uniaxial deformation in this study, a clear ⟨110⟩ fibre is shown to develop parallel to the tensile axis at $\psi = 90^\circ$ and $\psi = 270^\circ$ in Fig. 13(a). This development is produced at the expense of an initially strong ⟨111⟩ texture at $\psi = 90^\circ$ and $\psi = 270^\circ$, as shown in Fig. 13(d).

Uniaxial compression perpendicular to the plane of the sheet can be considered analogous to a balanced biaxial tension in the plane of the sheet due their equivalent effective stress states. Therefore texture change is expected in the ⟨111⟩ direction. This is indeed evident when observing the {222} reflection intensity during biaxial deformation. The macroscopic strain perpendicular to the plane of the loaded sheet would be the largest strain component, producing the preferred ⟨111⟩ texture. For the observed grains, in the plane of the sheet, the converse is observed; showing an expected reduction in {222} reflection intensity parallel to the tensile axes, thus confirming development of a ⟨111⟩ fibre texture perpendicular to the sheet. This is evident in both the $\epsilon_{TD}/\epsilon_{RD} = 1.5$, Fig. 13(l), and $\epsilon_{TD}/\epsilon_{RD} = 0.4$ test, Fig. 13(h), strain states.

5. Summary

1. A unique biaxial loading mechanism has been designed and built to enable, for the first time, in situ deformation of sheet metal whilst acquiring complete Debye–Scherrer X-ray diffraction data. Cruciform specimens with geometry suitable for deformation with high plasticity have been successfully made from FE designs simulated by Yu et al. [19].
2. The deformation at three strain ratios of a single phase ferritic, low carbon steel has been studied including (1) uniaxial, (2) $\epsilon_{TD}/\epsilon_{RD} = 0.4$ biaxial deformation, and (3) $\epsilon_{TD}/\epsilon_{RD} = 1.5$ (approximately balanced) biaxial deformation.
3. The distribution of lattice strain with respect to azimuthal angle is found to be highly dependent on the applied biaxial strain ratio. Whilst diffraction rings for uniaxial deformation distort, as expected from lattice strain increase in the tensile direction and reduction in the Poisson direction, lattice strain remains tensile in all measured orientations during biaxial deformation.
4. Deformation with a strain ratio close to balanced biaxial has shown that lattice strain initially accumulates more rapidly in the direction of the tensile axis with the greatest load, though the distribution becomes uniform at high plastic strain, irrespective of the strain ratio differing somewhat from $\epsilon_{TD}/\epsilon_{RD} = 1$.
5. Measurement of the integrated reflection intensity has been used to indicate texture changes during the differing applied strain states. Texture development was observed in both uniaxial and biaxial deformation, providing evidence of ⟨110⟩ and ⟨111⟩ fibre textures respectively.

Acknowledgements

Funding has been provided by EPSRC (Grant EP/I021043/1) with material and guidance from BMW-MINI gratefully acknowledged. With thanks also to the Diamond Light Source for the allocation of beamtime EE9333-1 on the I12 instrument and to Hamidreza Abdolvand for his assistance during the experiment.

References

[1] M. Fitzpatrick, A. Lodini (Eds.), Analysis of Residual Stress by Diffraction using Neutron and Synchrotron Radiation, Taylor & Francis, London, UK, 2003.
[2] A. Schwartz, M. Kumar, B. Adams, D. Field, editors. Electron Backscatter Diffraction in Materials Science, second ed., Springer, New York, USA, 2009.
[3] R. Dinnebier, S. Billinge (Eds.), Powder Diffraction Theory and Practice, The Royal Society of Chemistry, Cambridge, UK, 2008.
[4] A. Wilkinson, G. Meaden, D. Dingley, Ultramicroscopy 106 (2006) 307–313.
[5] J. Pang, T. Holden, J. Wright, T. Mason, Acta Mater. 48 (2000) 1131–1140.
[6] H.V. Swygenhoven, S.V. Petegem, Mater. Charact. 78 (2013) 47–59.

[7] M. Obstalecki, S.L. Wong, P. Dawson, M. Miller, Acta Mater. 75 (2014) 259–272.
[8] A. Makinde, L. Thibodeau, K. Neale, Exp. Mech. 32 (1992) 138–144.
[9] S. Ackermann, D. Kulawinski, S. Henkel, H. Biermann, Int. J. Fatigue 67 (2014) 123–133.
[10] G. Geandier, D. Thiaudière, R.N. Randriamazaoro, R. Chiron, S. Djaziri, B. Lamongie et al. Rev. Sci. Instrum. 81(10):eid103903, 2010.
[11] J. Repper, M. Niffenegger, S.V. Petegem, W. Wagner, H.V. Swygenhoven, Mater. Sci. Forum 768–769 (2013) 60–65.
[12] T. Marin, P. Dawson, M. Gharghouri, R. Rogge, Acta Mater. 56 (2008) 4183–4199.
[13] J. McNaney, V. Imbeni, Y. Jung, P. Papadopoulos, R. Ritchie, Mech. Mater. 35 (2003) 969–986.
[14] T. Gnaeupel-Herold, H. Prask, R. Fields, T. Foecke, Z. Xia, U. Lienert, Mater. Sci. Eng. A 366 (2004) 104–113.
[15] Z. Marciniak, K. Kuczyński, Int. J. Mech. Sci. 9 (1967) 609–620.
[16] M. Iadicola, T. Gnäupel-Herold, Mater. Sci. Eng. A 545 (2012) 168–175.
[17] BMW AG Group Standard, Cold-rolled DP steels (GS 93005–11). Technical Report, 2009.
[18] M. Brieu, J. Diani, N. Bhatnagar, J. Test Eval. 35 (2007) 1–9.
[19] Y. Yu, M. Wan, X.D. Wu, X.B. Zhou, J. Mater. Process. Technol. 123 (2002) 67–70.
[20] M. Hart, M. Drakopoulos, C. Reinhard, T. Connolly, J. Appl. Cryst. 46 (2013) 1249.
[21] FIT2D. <http://www.esrf.eu/computing/scientific/FIT2D/> (accessed March 2014).
[22] Gottingen: LaVision GmbH, DaVis. User's Manual. 2012.
[23] M. Mostafavi, D.M. Collins, B. Cai, R. Bradley, R.C. Atwood, C. Reinhard, X. Jiang, M. Galano, P.D. Lee, T.J. Marrow, Acta Mater. 82 (2014) 468.
[24] R. Dutta, R. Huizenga, M. Amirthalingam, A. King, H. Gao, M. Hermans, et al., Scripta Mater. 69 (2) (2013) 187–190.
[25] J. Nye, Physical Properties of Crystals, Oxford University Press, 1957.
[26] E. Oliver, M. Daymond, P. Withers, Acta Mater. 52 (2004) 1937–1951.
[27] M. Daymond, H. Priesmeyer, Acta Mater. 50 (2002) 1613–1626.
[28] G. Dieter, Mechanical Metallurgy, McGraw-Hill, 1988.
[29] U. Kocks, C. Tomé, H.R. Wenk, Texture and Anisotropy, Cambridge University Press, Cambridge, UK, 1998.